Chemical Science

Accepted Manuscript

This article can be cited before page numbers have been issued, to do this please use: F. Chen, Y. Xie, Z. Yu, N. Li, X. Ding and Y. Qiao, *Chem. Sci.*, 2026, DOI: 10.1039/D5SC08536E.

ROYAL SOCIETY OF CHEMISTRY

rsc.li/chemical-science

View Article Online
DOI: 10.1039/D5SC08536E

ARTICLE

Robust Janus-Faced Quasi-Solid-State Electrolytes Mimicking Honeycomb for Fast Transport and Adequate Supply of Sodium Ions

Received 00th January 20xx,
Accepted 00th January 20xx

DOI: 10.1039/x0xx00000x

Fang Chen,[a] Yadan Xie, [a] Zhoubin Yu,[a] Na Li,[a] Yu Qiao[b]* and Xiang Ding [c]*

Quasi-solid-state electrolytes are one of the most promising alternative candidate for traditional liquid state electrolytes with fast ion transport rate, high mechanical strength and wide temperature adaptation. Here we designed a biomimicking electrolyte film with a Janus-faced honeycomb-like structure and apply it to sodium ion batteries. The advanced quasi-solid-state sodium ion batteries come out with an initial coulombic efficiency of 105% and stable charge-discharge cycles in a wide temperature range from -20 ℃ to 60 ℃. Also, operando observations on chemical structure and interfacial evolution have been operated to exhibit a robust and stable quasi-solid-state electrolyte film.

Introduction

A revolution from traditional liquid electrolytes to quasi-solid-state electrolytes, and then to all-solid-state electrolytes has been under way for alkali metal ion batteries that aim to push beyond the limits of energy density.[1-4] Quasi-solid-state electrolytes (QSSE), namely gel electrolytes, have been considered as one of the most promising candidates for next-generation rechargeable batteries for possessing tremendous chemical, mechanical and electrochemical merits. QSSEs have improved mechanical flexibility, alleviated solution leakage, enhanced cycling stability, extended working potential window and so on, compared with liquid electrolytes.[5-7] In contrast with all-solid-state electrolytes, gel electrolytes address issues like poor interfacial contact, high operating temperature, relatively low room-temperature conductivity, etc.[8, 9] Moreover, QSSEs with polymer matrix are expected to demonstrate more functionalities and possibilities than merely ion transport assisted with ingenious design.[10, 11] For instance, gel electrolytes with flexibility, widened operating temperature and safety insurance so far have been developed and applied for lithium ion batteries (LIBs). Nevertheless, as a potential alternative to LIBs, sodium ion batteries (SIBs) with multi-functional QSSEs have remained an underdeveloped project and demand further exploration for more possibilities.[12-14]

Although research on SIBs can be dated back to 1960s, similar to LIBs (1970s), there still remain practical problems to solve and electrochemical properties to perfect.[15, 16] For instance, the thermodynamics and kinetics for growth of sodium dendrites have not yet been fully understood since it differs largely from lithium dendrites.[17] Nevertheless, sodium dendrites could trigger severe damage to cells by consuming electrolytes, increasing impedance and even worse, penetrating the separators which leads to short circuit. According to previous researches[18-21], sodium dendrites have higher plastically complaince and more unstable SEI growth than lithium dendrites. Therefore, it is necessary to suppress the growth of sodium dendrites for stable and safe SIBs.[22] Strategies have been proposed that involve optimized electrolytes and interfacial engineering. An electrode-electrolyte interface with enhanced mechanical strength to prevent dendrites is confirmed to be effective and efficient.[23] As for the cathode side, a trade-off between high capacity and stable cycling performance is tricky to make. Taking Prussian blue analogues (PBAs), eg., $Na_{2-x}Fe[Fe(CN)_6]$, as an example, they have a high theoretical specific capacity of 171 mAh g^{-1} (x=0), yet current reversible capacity is often below 120 mAh g^{-1} owing to sodium deficiency. Sodium deficiency also affects cycling stability because high sodium contents correspond to a rhombohedral crystal structure, which has a higher structural stability through charge-discharge cycles than a cubic phase.[24, 25] Modifications on the fabrication process is the most popular way to synthesize PBAs with sufficient Na proportion, which requires delicate operation or inappropriate waste of raw materials.[26] Gel electrolytes have been considered as an option broadening temperature range and resisting fire for sodium ion batteries. For thermal stability, Xiu-Li Wang and his coworkers have incorporated diethyl vinylphosphonate (DEVP) into PAN polymer matrix for high temperature stability. And the film can sustain its shape when the temperature rises to 180 ℃.[27] Also, phosphorus and fluorine are supposed to extinguish fire and inhibit

[a] Zhejiang Baima Lake Laboratory Co., Ltd., 310052 Hangzhou, Zhejiang, China.
[b] State Key Laboratory of Physical Chemistry of Solid Surfaces, Discipline of Intelligent Instrument and Equipment, College of Chemistry and Chemical Engineering, Xiamen University, Xiamen 361005, China;
[c] College of Chemistry and Materials Science, Fujian Normal University, Fuzhou, 350007, China;
[d]
Email: Yu Qiao, yuqiao@xmu.edu.cn; Xiang Ding, dingx@fjnu.edu.cn.

further spreading for polymer electrolytes, and agents like tri(acryloyloxyethyl) phosphate (TAEP) are proved to be efficient.[28]

Herein, we propose a multi-functional gel electrolyte with a Janus-faced structure fabricated via phase inversion, one 'face' to suppress sodium dendrites and another to supply sodium ions and buffer free electrolytes. As for a high-performance QSSE, microscopic structure is supposed to have abundant cavities to store electrolyte solution and densely arranged shared walls to resist external stress. The synthesized QSSE film has a spontaneously-formed morphology that resembles honeycombs in nature and consequently attains high flexibility and plasticity. To support as much honey and pollen as possible, as well as sustain integrity, natural honeycomb has aligned hives with shared sides for bees to work on and brood in. The honeycomb-like Janus-faced (HJ) QSSE has been introduced into sodium ion batteries, exhibiting a sodium-ion diffusion rate comparable to that of liquid electrolytes. The HJ film has demonstrated outstanding thermal stability (maintain its shape at 300 ℃) and self-extinguishing ability. The assembled quasi-solid-state sodium ion batteries demonstrate a superior sodium storage capability with an initial capacity of 130 mAh g^{-1}, 90% capacity retention after 700 charge-discharge cycles and robust charge-discharge performance in a wide temperature range. Also, assisted by operando tests, the stability of crystal chemical structures and interfacial properties have been demonstrated with operando evidence.

Experimental Section

Synthesis of HJ film: Poly (vinylidene fluoride-co-hexafluoropropylene (PVDF-HFP) was purchased from Shanghai Macklin Biochemical Technology Co., Ltd, average Mw: 40,000, pellets. Molecular sieve ZSM-5 was got from SINOPEC shanghai research institute of petrochemical technology co., ltd, powders. 1-Methyl-2-pyrrolidinone (NMP) was purchased from Shanghai Macklin Biochemical Technology Co., Ltd, >99.0%.

1. Preparation of 10% PVDF-HFP solution. 2 g PVDF-HFP and 18 g NMP were added in a glass bottle with a magneton, and then the solution was stirred till fully dissolved (~4 h) at room temperature.

2. Preparation of the precursor solution. Taking certain amount of ZSM-5 into the above-mentioned solution. The amount of ZSM-5 can be varied from 3 g (PVDF-HFP: ZSM-5=4:6) to 4.7 g (PVDF-HFP: ZSM-5=3:7) according to our experimental results. The ration of PVDF-HFP: ZSM-5 can be deceased to 1:9 with extra amount of NMP added.

3. Preparation of HJ film. First, the solution was covered (20×8 cm^2) in the surface of a piece of glass with the aid of a scraper. The thickness of the scraper is 100 μm, and increased 1000 μm to for the Operando optical microscopy experiment. Then the glass was put into a container with 600 mL deionized water in it and kept for 6 h for solution exchange at room temperature. After that the film was taken out and put into an oven, drying at 110 °C for 24 h with a vacuum pumping.

Synthesis of PBA cathode: The synthesis process of PBA powders follows the same route of previously reported article via a co-precipitation way[29]. Then the PBA powders was mixed with super P and PVDF with a ratio of 8:1:1 with certain amount of NMP. Then the slurry was scraped on an Al foil with a thickness of 100 μm. The the film was dried at 80 ℃ in an oven with a vacuum pumping. Then the cathode film was cut into appropriate sizes as needed.

Characterization: Crystal structure of materials were determined with a D8 ADVANCE X-ray diffractometer by a Cu Ka radiation line (λ=1.5418 Å). SEM images were taken by SEM5000X from Chinainstru & Quantumtech (Hefei) Co., Ltd. The TGA analysis was carried out by a Sdt Q600 V20 9 Build 20 Thermal Gravimetric Analyzer with a scanning rate of 10 °/min.

Electrochemical test: A quasi-solid-state cell was assembled with a piece of cathode flim, HJ film swollen with liquid electrolytes (1 M $NaClO_4$ in PC/EC/FEC: 45:45:10) and sodium metal foil The control sample was assembled with HJ film replaced as glass fiber (GF). The galvanostatic charge-discharge experiments were carried out in a LAND CT3002A multichannel battery test system. The cyclic voltammetry (CV) tests (Potential window: 2-4 V) and electrochemical impedance spectroscopy (EIS, 10^{-2} Hz to 10^5 Hz with an amplitude of 5 mV) were operated with a CHI 660E workstation. Operando optical microscopy experiment was operated with an Operando Confocal Microscopy assisted with a LAND CT3002A.

Results and Discussions

In QSSEs, electrolyte solution exists in different forms, either swollen by polymers or filling microscopic pores. Consequently, a higher porosity translates into a larger electrolyte uptake.[30] A porous structure with regular aligned pores can sustain external compression. Conversely, a dense structure with fewer pores means less contact between liquid electrolyte solution with the electrode and less side effects the same time. Therefore, making a trade-off of the proportion and distribution of microscopic pores is tricky, yet of importance. In this work, a phase inversion process is utilized to fabricate an asymmetric membrane consisting of a polymer-rich skin layer and a polymer-lean porous sub-layer that combine high mechanical strength with excellent electrochemical performance.

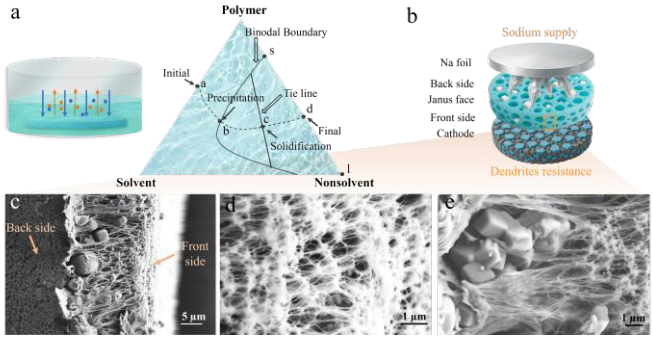

Figure 1. Schematic illustration of a) the synthesis process of HJ film and b) a cell with a Janus-faced gel electrolyte. Microscopic images of cross-sectional view of c) the entire section, d) the font side and e) the back side.

The synthesis process is depicted in Figure 1a, the solution containing polymers, a molecular sieve and solvent (NMP) was cast on a glass plate and put into a container with a nonsolvent for a solvent (DI water) exchange process. The membrane formation process is displayed in the ternary phase diagram on the right side in Figure 1a, and the dashed line abcd describes the evolution progress of the system. After being placed into the non-solvent, an instant solution exchange takes place and a thin-skin layer was formed. The binodal boundary line divides the diagram into a single-phase region and a binary-phase region. Thus, a transformation takes place at point b and the system breaks into two phases, the polymer-rich phase and polymer-lean phase, which finally evolves to the membrane matrix and the pore regions, respectively. Because solvent exchange is rapid at the film surface but sluggish in the bulk. The separation process is completed at point c. The final point d represents the final composition of the system with a certain ratio of membrane part (the point s stands for) and pore part (the point l stands for). Moreover, with the phase inversion process, the molecular sieve with higher hardness in the system would precipitate and gather in the bottom and has a gradient concentration from the bottom to the top. After the non-solvent removed, the membrane shows a distinct morphology with a dense front side, a hard back side and a porous inner layer in between. Optical images in Figure S1 shows that the HJ film turns to semi-transparent after swollen with electrolyte solution. Also, the surface exhibits a typical Turing pattern. A quasi-solid-state sodium ion cell was assembled with the back side of the HJ gel electrolytes facing the sodium metal and the front side facing the cathode, as displayed in Figure 1b. The cross-section area was magnified and demonstrated via SEM images in Figure1c-e. The cross-section area presents a sponge-like porous structure, which is supposed to accommodate electrolyte solution and resist compression. Inorganic particles clustered on the back side owing to gravity, and this dense layer could resist sodium metal dendrite penetration, functioning as a safety proof. The structure is relatively dense on the front side to minimize electrolyte contact with the cathode, suppressing side reactions and extending cycle life.

Chemical structures, microstructures and physical properties of synthesized HJ film have been characterized. As shown in Figure 2a, the molecular sieve (ZSM-5) in the film is indexed to a tetragonal phase, space group of $p4_221_2$, identified by a standard diffraction pattern of JCPDS#00-044-000. Cations existed in this molecular structure are sodium ions, supplying extra sodium ions for the sodium ion batteries. Moreover, ZSM-5 is a 5 Å-type molecular sieve, providing channels with radius of ~0.5 nm, which is sufficient for solvated sodium ions (stokes radius for Na^+: ~4.6) to pass through. By contrast, the XRD pattern of a piece of HJ film has an extra broad peak from 15° to 30° (Figure S2), showing that the PVDF-HFP has an amorphous phase in the film. Thermostability of the HJ film (Figure S3a) and a piece of commercialized PE separator (Figure S3b) were tested and compared by thermal analysis. The decomposition temperature increased from 260 ℃ to 440 ℃ for the HJ film compared with the PE film, indicating a significant improvement for HJ films. After 600 ℃, PE film was completely decomposed, while only PVDF-HFP part of the HJ film has been decomposed and the rest part (molecular sieve) can survive the high temperature.

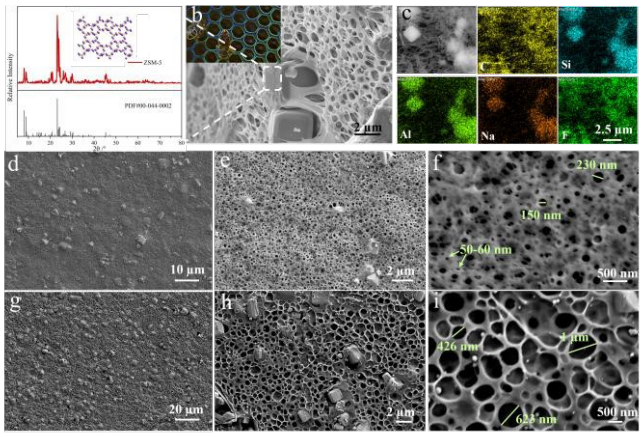

Figure 2. a) XRD pattern of molecular sieve ZSM-5. b) SEM images of honeycomb-like structure, insert picture: natural honeycomb. c) Element mapping of the HJ film. d-f) Front side view of HJ film with different magnification. g-i) Back side view of HJ film with different magnification.

As displayed in Figure 2b, the microstructure of the HJ film resembles the pore alignment of a honeycomb, which is constructed with less material, higher porosity and high strength. Owing to structural superiority, the HJ film is able to lift heavy load more than 2000 times its own weight, as shown in Figure S4. Also, the film is bendable and stretchable in Figure S5. Figure 2c reveals element distribution, including C, Si, Al, Na and F, on the surface of a piece of HJ film. ZSM-5 has element C (absorbing organics), Si and F, and PVDF-HFP has element C and F, corresponding to the mapping result. Two faces of the HJ film show different morphologies, via a comparison of SEM images of the front side (Figure 2d-f) and the back side (Figure 2g-i) with different magnifications. As clearly seen from Figure 2d and 2g,

View Article Online
DOI: 10.1039/D5SC08536F

there're more molecular sieve particles in the back side than the front side from the overall view, which can be verified in Figure 2e and Figure 2h. Different kinds of pore distributions have been vividly exhibited in Figure 2f and Figure 2i, showing the distinctive features of skin layer and sponge layer. In the front side, pores generally have a diameter below 300 nm, mostly around 100 nm, showing a dense structure. Contrary to the front side, most pores have diameters above 400 nm on the back side, and the shared walls are thin, identical to structures of sponges. As in Figure S6, the pore sizes can be modified by changing the volume of the non-solvent, water, probably due to a change of solvent exchange rate. With lower ratio of DI water (from 600 mL to 400 mL), pores have an increased diameter around 400 nm on the front side. Less water in the system could result in a slowed-down solvent exchange process, thus a relatively less compact structure is produced. Also, the ratio of ZSM-5 to PVDF-HFP can be modulated in a wide range from 0 to 9:1 to ensure the integrity of a film. As shown in Figure S7, the film with the ratio of 9:1 still has a porous structure which is constructed by stackings of inorganic particles. However, the film loses its bendability with a high concentration of ZSM-5.

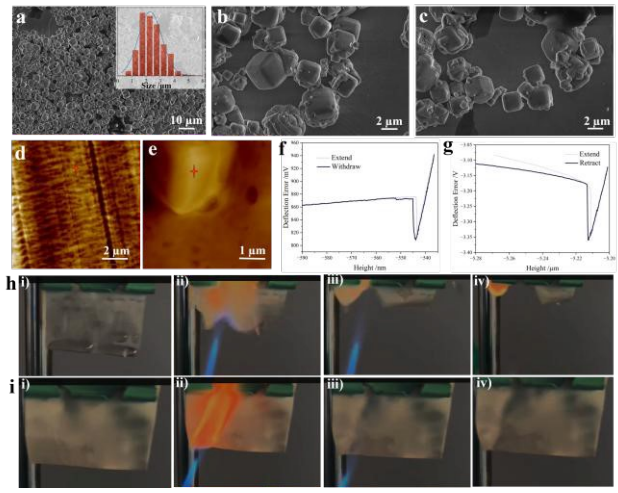

Figure 3. Robustness of HJ film. a-c) SEM images of ZSM-5 particles with different magnitudes. Atomic force microscopic images of d) conventional PE film and e) HJ film. Approach and retrace examination of f) conventional PE film and g) HJ film. Ignition tests of h) conventional PE film and i) HJ film with butane.

Figure 3a-c display an overview of ZSM-5 particles incorporated into the HJ film. As calculated by statistic data, the particles have a relatively uniform size distribution with a diameter of 2.288±0.065 μm. To examine mechanical strength on the surface on a microscopic basis, approach-retrace tests have been conducted with atomic force microscopy. A conventional PE film is utilized as a contrast sample in the examination, and the image in Figure 3d has shown fabric morphology with interwind fibers. Figure 3e shows a cubic particle inlayed in the PVDF-HFP matrix, the same structure as mentioned above. Quantitative nanomechanical mapping tests are implemented in a selected area marked with a red star shown in Figure 3d, 3e. As a comparison, HJ film has a peak force four times higher than the PE film, showing high rigidity to resist the penetration of sodium metal. Also, seen from the slope in the repulsion part, the HJ film has an elastic modulus ten times higher than the PE film, which determines a robust surface. Apart from mechanical robustness, tests on thermal stability and fire resistance of the HJ film have been shown in Figure 3h, 3i and Figure S8. As shown in Figure 3h, 3i, both films can be lit within 0.1 s with butane. However, the fire continues once the source of fire is removed for PE film, while the fire is self-extinguished and the film maintains its shape after the fire is withdrawn. The self-distinguish behavior of the HJ film is properly due to high concentration of molecular sieve and the existence of element F. To test high temperature stability for our film, two samples, a piece of PE film and HJ film have been placed on a heat conductor and the temperature has been set from room temperature to 300 ℃. PE film tends to deform above 110 ℃ and melts at 147 ℃. Differ from PE film, the HJ film has sustained its shape even at 300 ℃, showing a superior thermal stability. On a cell basis, the battery with PE as the separator faces issues like short circuit when exposed to fire or heat.

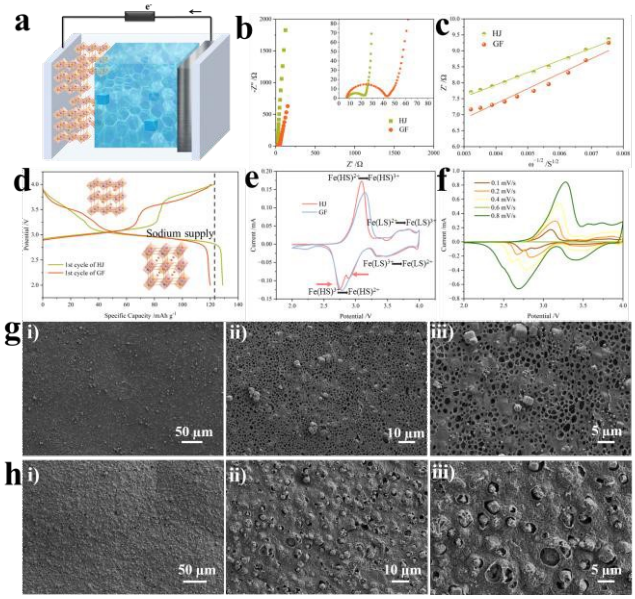

Figure 4. Characterization of charge transferring and diffusion. a) Schematic illustration of mechanism of quasi-solid-state sodium ion batteries. b) Nyquist plots and c) plots of corresponding Z' versus ω−1/2 in the low frequency region of quasi-solid-state and liquid-state SIBs. d) Initial charge and discharge curves and e) CV curves of SIBs with HJ QSSEs and glass fiber. f) CV curves of SIBs with HJ QSSEs at different scanning rates. SEM images of the surface towards sodium metal g) before and h) after charge-discharge cycles.

Quasi-solid-state electrolytes have the ability to confine electrolyte solution by swelling with liquids, so they are reported to enhance the stability and alleviate liquid leakage problems of rechargeable batteries. For battery tests, the weight ratio of liquids in the gel electrolytes is 30%-40%. Besides, the conductivity of QSSEs reaches the order of magnitude of liquid electrolytes. As drawn in Figure 4a, a quasi-solid-state cell was assembled with a piece of Prussian blue analogue (PBA)-based cathode, QSSE and sodium metal foil. The PBA particles were synthesized as previously reported, and have a stacked cubic structure as Figure S9 presents. The chemical

View Article Online
DOI: 10.1039/D5SC08536E

composition is identified as $Na_{1.53}Fe[Fe(CN)_6]$ and the crystal structure is confirmed to be a sodium-deficient cubic phase as reported. Nyquist plots of QSS (HJ) and liquid-state (glass fiber, GF) sodium ion batteries have been demonstrated in Figure 4b for comparison. Contact resistance of the HJ-based sample (7.7 Ω) is approaching the one of GF-based (7.2 Ω), indicating a good interfacial contact between the electrodes and QSSE. Also, charge transfer resistance reduces from 18.0 Ω to 7.5 Ω thanks to joint efforts of structural and chemical compositional design. The diffusion resistances of the two samples are characterized by the slopes of fitting lines in Figure 4c. Generally, a steeper line suggests a higher resistance. Therefore, the cell with HJ has improved sodium ion transport dynamics compared with the one with GF. The conductivity of HJ film has been calculated to be 7.8×10^{-3} S cm^{-1}. Also, a steady-state current measurement and impedance spectra before and after polarization on a sodium metal symmetrical cell have been shown in Figure S10. The current response was obtained with an amplitude of 50 mV, and the transference number of sodium ions has been determined as 0.70.

Cubic phase Na-deficient Fe-based PBAs have been reported to have an unstable cycling performance in 200 cycles owing to poor crystallinity. Moreover, the cubic phase with low concentration of Na cannot be restored after deintercalation of sodium ions.[31] However, in our case, with the Na-type sieve-embedded HJ gel electrolytes, more sodium ions would intercalate back to the framework of PBAs than how many they deintercalated from. As depicted in Figure 4d, the coulombic efficiency of the initial charge-discharge cycle is more than 100% for the HJ-based sample, and the first discharge capacity reaches 130 mAh g^{-1} at a current density of 0.1 C. Also, the discharge platform in the relatively lower potential range has been prolonged compared with the GF-based sample. Figure 4e shows the CV curves of two samples at a scanning rate of 0.1 mV/s. Based on the distance between the oxidation peak and reduction peak, the polarization has been minimized for HJ-based sample. Redox peaks at a lower potential are responsible for high-spin Fe^{2+}/Fe^{3+} that is connected with N sites and the peaks at a higher potential correlates with low-spin Fe^{2+}/Fe^{3+} that is connected with C sites. As revealed by the distance between the oxidation peaks and reduction peaks of high-spin Fe^{2+}/Fe^{3+}, HJ-based battery has a minimized polarization. Also, the reduction peak in the range of 2.5-4.2 V has been split into two peaks, and this phenomenon has disappeared when the scanning rate increases to 0.8 mV/s, as displayed in Figure 4f. The CV curves maintain their shapes when the scanning rate rises from 0.1 mV/s to 0.8 mV/s, indicating an excellent rate performance. To elucidate the role of the HJ film, post-cycling SEM and XPS analyses were performed. Figures 4g and 4h compare the anode-side surface of the HJ film before and after cycling at different magnifications. The images reveal significant pore shrinkage and the formation of a dense surface layer after cycling. Furthermore, an additional peak at 288.3 eV in the C 1s spectrum, assigned to C=O (Figure S11), confirms electrolyte decomposition on the HJ film.

The phase transition process through a charge-discharge cycle of QSSE-based sodium ion batteries is revealed by an in-situ XRD test in Figure 5a. Three peaks at 22.8°, 23.0° and 23.5° are attributed to ZSM-5 in the gel electrolytes. The three peaks remaining at fixed position verifies that molecular sieve ZSM-5 retains its crystal structure which is mainly constructed by Si and Al during the charge-discharge procedure. Figure S12 shows the XRD pattern of the PBA-based cathode, and the peaks are identified as reflections from the (200), (220), (400) and (420). While the cell was charged, a peak shifting towards higher angle has been detected at 16.8° and 34.2°, assigned to a shortened inter-planar spacing of the (200) and (400) for PBA-based cathode. Besides, the appearance of an extra line at 24.4° , as well as at 39.2°, indicates that parts of PBAs transformed to rhombohedral phase.[32] The peaks return to their initial positions after discharging back to 2.0 V, implying a reversible phase transformation through a single charge-discharge cycle.

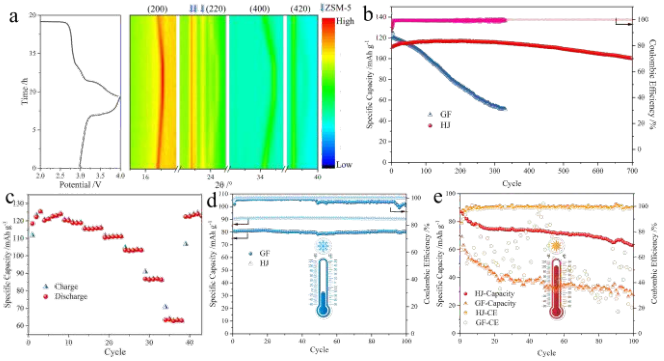

Figure 5. Stability for the HJ-based quasi-solid-state SIBs at ambient, low and high temperature. a) In-situ XRD pattern of quasi-solid-state SIBs: PBAs | HJ QSSEs | Na. b) Comparison of cycling stability of SIBs with HJ and glass fiber. c) Rate performance of quasi-solid-state SIBs. 0.1 C for three cycles, then 0.2 C, 0.3 C, 0.5 C, 1 C, 2 C, 5 C, 10 C and 0.2 C for five cycles. Charge-discharge cycles for quasi-solid-state liquid-state SIBs at d) -20 ℃ and e) 60 ℃. The cycling stability tests were all carried out at 1 C after activated at 0.1 C for three cycles.

On account of the integrity of chemical structure, suppressed electrolyte solution corrosion and stabilized electrolyte-electrode interface, the HJ-based cell exhibits excellent cycling stability in a wide temperature range, from -20 ℃ to 60 ℃. Cycling performance at room temperature or in a wide temperature range has been investigated for polymer electrolytes. Hong Jin Fang et al. have applied double-layer polymer electrolytes for stable sodium ion batteries with 80.4 mAh g^{-1} capacity after 400 cycles at 1 C (room temperature).[33] Guanglei Cui et al developed a smart gel polymer electrolyte and applied it for sodium ion batteries with 80% capacity retention after 500 cycles at 50 ℃.[34] Cycling performance at 25 ℃ has been displayed in Figure 5b. The GF-based cell has a dramatic capacity drop after 100 charge-discharge cycles, and has a low capacity retention of 43% after 300 cycles, mainly due to collapse of the crystal structure of PBAs, side reactions in electrolytes and so on. The cell experiences a large potential drop through the long-cycle test, from 0.085 V (1^{st} cycle) to 0.48 V (100^{th} cycle) and 0.76 V (300^{th} cycle), as shown in Figure S10b. Also, GF-based SIB has a coulombic

efficiency drifts markedly after 200 cycles, which is owing to side effects and electrolyte exhaustion. For HJ gel-based SIB, the capacity slowly increases for the first 100 cycles, probably due to a sodium ion supply process. The capacity retention reaches 90% even after 700 cycles and the coulombic efficiency stays above 99.9% through the whole process. Figure S13a shows that no obvious potential drop occurs after cycling tests. Figure 5c displays the rate performance at a current density from 0.1 C to 10 C at ambient temperature. HJ-based quasi-solid-state SIBs demonstrate an outstanding fast sodium ion storage capability, with a capacity of 60 mAh g^{-1} even at a current density of 10 C. Polymers are reported to enhance anti-freezing ability for liquids. Therefore, the capacity remains 90 mAh g^{-1} for gel electrolytes, while the capacity drops to 80 mAh g^{-1} for liquid electrolytes at 1C. Potential drops of charge-discharge curves in Figure S14 also corroborate that the gel-based batteries have improved conductivity. When the temperature decreases to -20 ℃, both HJ-based and GF-based cells show high capacity retentions of 101% and 99%, respectively for 100 charge-discharge cycles, as displayed in Figure 5d. However, after 50 cycles the coulombic efficiency has dropped to around 96%. Sodium dendrites remain troublesome at a sub-zero temperature, and they consume a large amount of electrolyte solution. For the HJ-based cell, the coulombic efficiency maintains above 99.9%. Liquid electrolytes are intolerant to high temperature for solvent evaporation and accelerated undesired reactions.[35] As a result, in Figure 5e GF-based SIB exhibits an extremely unstable electrochemical performance at 60 ℃, shown by the coubombic efficiency. Also, the capacity drops to below 40 mAh g^{-1} after 20 cycles. On the other hand, the coulombic efficiency for HJ-based SIB has a stable coulombic efficienct around 100%, and the capacity retention is 73% after 100 cycles. The charge-discharge curves of the initial and 100th cycle have been displayed in Figure S15. Overall, HJ-based QSSEs are capable of withstanding temperature variations in the environment.

Thermodynamics and kinetics of the growth of sodium dendrites have remained a project requiring further exploration. However, it is commonly recognized that sodium metal has an unstable solid electrolyte interphase, high reactivity with the electrolyte and non-uniform dendrite growth. Operando confocal microscopy has been applied under galvanostatic conditions to observe the dendrite growth for a quasi-solid-state SIB and a liquid-state SIB in Figure 6. Observation has been conducted at a current density of 0.1 C and 1 C, respectively, and the charge-discharge curves are shown in Figure 6a. Confocal microscopic videos have been taken through a view concentrating on the gel electrolyte or glass fiber, which is drawn in Figure 6b.

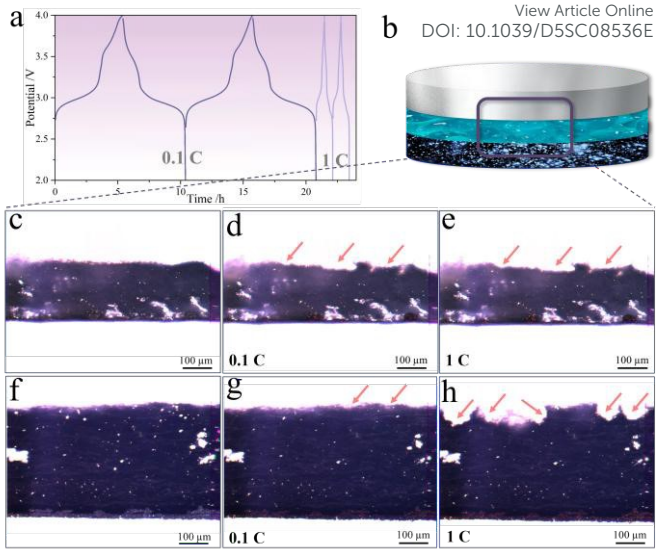

Figure 6. Operando microscopic observation of quasi-solid-state and liquid-state SIBs on operation. a) Charge and discharge curves of SIBs at different current densities. b) Schematic illustration of the observation view. c) Initial and d) charged at a current density of 0.1 C and e) charged at 1 C of quasi-solid-state SIBs. c) Initial and d) charged at a current density of 0.1 C and e) charged at 1 C of liquid-state SIBs.

The evolution process through charge-discharge process is displayed in Figure S16 by screen shots from video S1. Sodium metal dendrites would grow at different positions when charged to different voltages. When discharged, some parts of sodium metal dendrites would size down and redissolve into sodium ions. The sodium metal dendrites have mossy-like appearance. Sodium metal dendrites at different current densities of HJ-based quasi-solid-state SIB were compared with GF-based liquid-state SIB, and the results are shown in Figure 6c-e (from Video S1) and Figure 6f-h (from Video S2). As shown in Figure 6c-e, the penetration of sodium dendrites would be hindered when the rate increased from 0.1 C to 1 C. Therefore, the risk of short circuit and other hazards such as electrolyte consumption, dead sodium, etc. have been minimized. In contrast, sodium dendrites have clearly penetrated deeper into the glass fiber when the rate rises, seen from Figure 6f-h. The substantial improvement partly is attributed to the hardness of the surface with abundant ceramic particles. Besides, limited amount of electrolyte and the sodiophilic nature of the molecular sieve also contributes to the improved performance. [36]

Conclusions

We have fabricated a quasi-solid-state electrolyte film with a spontaneously formed Janus-faced honeycomb-like structure. With the joint efforts of polymer and molecular sieve, the film is flexible, bendable, robust and of high conductivity for sodium ions. When applied to sodium ion batteries, the as-obtained electrolyte has demonstrated its superiority in constraining

extra liquid solvent and supplying sodium ions. The HJ-based quasi-solid-state SIB has achieved excellent performance with long-term cycle stability of 90% capacity retention and a stable coulombic efficiency of over 99.9% after 700 cycles. The mechanism for outstanding electrochemical stability has been revealed by in-situ XRD measurements and operando confocal microscopic observation. Evidence has testified that the PBA-based cathode experiences a cubic-to-rhombohedral phase transition partially; furthermore, the phase transition and crystal structure expansion process are entirely reversible. The growth of sodium dendrites has been suppressed, especially for large current density, which contributes to high safety, high coulombic efficiency as well as long cycle life. Moreover, the special structure design has broadened the temperature range it adapts to from -20 ℃ to 60 ℃. The multi-functional QSS electrolytes have more to explore than presented in this paper, and we hope these findings will inspire further research.

Conflicts of interest

There are no conflicts to declare.

Acknowledgements

This work is financially supported by Department of Science and Technology of Zhejiang Province (Grant number: 31941023072).

References

1 H. Pourzolfaghar, P.-Y. Wang, X.-Y. Jiang, S. Kositsarakhom, W. Jirasupcharoen, C. Suwantri, D. Jyothi, K. Prabhakaran and Y.-Y. Li, Emerging trends and innovations in all-solid-state lithium batteries: A comprehensive review, *Chemical Engineering Journal*, 2024, **500**, 157394.
2 Z. Cheng, T. Liu, B. Zhao, F. Shen, H. Jin and X. Han, Recent advances in organic-inorganic composite solid electrolytes for all-solid-state lithium batteries, *Energy Storage Materials*, 2021, **34**, 388-416.
3 H. Aziam, B. Larhrib, C. Hakim, N. Sabi, H. B. Youcef and I. Saadoune, Solid-state electrolytes for beyond lithium-ion batteries: A review, *Renewable and Sustainable Energy Reviews*, 2022, **167**, 112694.
4 J. Lu, Y. Chen, Y. Lei, P. Jaumaux, H. Tian and G. Wang, Quasi-Solid Gel Electrolytes for Alkali Metal Battery Applications, *Nano-Micro Letters*, 2025, **17**, 1-66.
5 K. Aruchamy, S. Ramasundaram, S. Divya, M. Chandran, K. Yun and T. H. Oh, Gel polymer electrolytes: advancing solid-state batteries for high-performance applications, *Gels*, 2023, **9**, 585.
6 X. Fan, C. Zhong, J. Liu, J. Ding, Y. Deng, X. Han, L. Zhang, W. Hu, D. P. Wilkinson and J. Zhang, Opportunities of flexible and portable electrochemical devices for energy storage: expanding the spotlight onto semi-solid/solid electrolytes, *Chemical Reviews*, 2022, **122**, 17155-17239.
7 P. Jaumaux, J. Wu, D. Shanmukaraj, Y. Wang, D. Zhou, B. Sun, F. Kang, B. Li, M. Armand and G. Wang, Non‐flammable liquid and quasi‐solid electrolytes toward highly‐safe alkali metal‐based batteries, *Advanced Functional Materials*, 2021, **31**, 2008644.
8 H. Huo and J. Janek, Solid-state batteries: from 'all-solid'to 'almost-solid', *National science review*, 2023, **10**, nwad098.
9 L. Mazzapioda, A. Tsurumaki, G. Di Donato, H. Adenusi, M. A. Navarra and S. Passerini, Quasi-solid-state electrolytes-strategy towards stabilising Li| inorganic solid electrolyte interfaces in solid-state Li metal batteries, *Energy Materials*, 2023, **3**, 1-3025.
10 J. Chattopadhyay, T. S. Pathak and D. M. Santos, Applications of polymer electrolytes in lithium-ion batteries: A review, *Polymers*, 2023, **15**, 3907.
11 D. Zhou, D. Shanmukaraj, A. Tkacheva, M. Armand and G. Wang, Polymer electrolytes for lithium-based batteries: advances and prospects, *Chem*, 2019, **5**, 2326-2352.
12 J. Zheng, W. Li, X. Liu, J. Zhang, X. Feng and W. Chen, Progress in gel polymer electrolytes for sodium‐ion batteries, *Energy & Environmental Materials*, 2023, **6**, e12422.
13 F. Gebert, J. Knott, R. Gorkin III, S.-L. Chou and S.-X. Dou, Polymer electrolytes for sodium-ion batteries, *Energy Storage Materials*, 2021, **36**, 10-30.
14 Z. Chang, H. Yang, X. Zhu, P. He and H. Zhou, A stable quasi-solid electrolyte improves the safe operation of highly efficient lithium-metal pouch cells in harsh environments, *Nature Communications*, 2022, **13**, 1510.
15 Y. Gao, H. Zhang, J. Peng, L. Li, Y. Xiao, L. Li, Y. Liu, Y. Qiao and S. L. Chou, A 30‐year overview of sodium‐ion batteries, *Carbon Energy*, 2024, **6**, e464.
16 P. K. Nayak, L. Yang, W. Brehm and P. Adelhelm, From lithium‐ion to sodium‐ion batteries: advantages, challenges, and surprises, *Angewandte Chemie International Edition*, 2018, **57**, 102-120.
17 F. Huang, P. Xu, G. Fang and S. Liang, In‐depth understanding of interfacial Na+ behaviors in sodium metal anode: migration, desolvation, and deposition, *Advanced Materials*, 2024, **36**, 2405310.
18 Y.-S. Hong, N. Li, H. Chen, P. Wang, W.-L. Song and D. Fang, In operando observation of chemical and mechanical stability of Li and Na dendrites under quasi-zero electrochemical field, *Energy Storage Materials*, 2018, **11**, 118-126.
19 A. Rudola, D. Aurbach and P. Balaya, A new phenomenon in sodium batteries: Voltage step due to solvent interaction, *Electrochemistry communications*, 2014, **46**, 56-59.
20 B. Yadav, C. B. Soni, S. Bera, H. Kumar and V. Kumar, Direct observation of sodium dendrites to decipher the complicated behavior of electrolyte systems, *Electrochimica Acta*, 2024, **507**, 145212.
21 B. Lee, E. Paek, D. Mitlin and S. W. Lee, Sodium metal anodes: emerging solutions to dendrite growth, *Chemical reviews*, 2019, **119**, 5416-5460.
22 H. Wang, E. Matios, J. Luo and W. Li, Combining theories and experiments to understand the sodium nucleation behavior towards safe sodium metal batteries, *Chemical Society Reviews*, 2020, **49**, 3783-3805.
23 T. Wang, Y. Hua, Z. Xu and J. S. Yu, Recent advanced development of artificial interphase engineering for stable sodium metal anodes, *Small*, 2022, **18**, 2102250.
24 W. Wang, Y. Gang, Z. Hu, Z. Yan, W. Li, Y. Li, Q.-F. Gu, Z. Wang, S.-L. Chou and H.-K. Liu, Reversible structural evolution of sodium-rich rhombohedral Prussian blue for sodium-ion batteries, *Nature communications*, 2020, **11**, 980.
25 J. Peng, W. Zhang, Q. Liu, J. Wang, S. Chou, H. Liu and S. Dou, Prussian blue analogues for sodium‐ion batteries: past, present, and future, *Advanced Materials*, 2022, **34**, 2108384.
26 S. Fan, Y. Liu, Y. Gao, Y. Liu, Y. Qiao, L. Li and S. L. Chou, The design and synthesis of Prussian blue analogs as a sustainable cathode for sodium‐ion batteries, *SusMat*, 2023, **3**, 749-780.

View Article Online
DOI: 10.1039/D5SC08536E

27 M.-C. Long, G. Wu, X.-L. Wang and Y.-Z. Wang, *Energy Storage Materials*, 2022, **53**, 62-71.
28 X. Mu, X. Li, C. Liao, H. Yu, Y. Jin, B. Yu, L. Han, L. Chen, Y. Kan and L. Song, Advanced Functional Materials, 2022, 32, 2203006.
29 F. Chen and C. Chen, Spontaneously formed ant-nest structure for binder-free sodium ion batteries with ultra-high electrode loading, Chemical Engineering Journal, 2023, **466**, 143327.
30 S. Zhou, Y. Yang, L. Shi, S. Zhang, J. Wang, F. Zhang and S. Zhao, Recent progress of gel-based materials in energy storage and conversion, *Materials Horizons*, 2025.
31 W.-J. Li, S.-L. Chou, J.-Z. Wang, Y.-M. Kang, J.-L. Wang, Y. Liu, Q.-F. Gu, H.-K. Liu and S.-X. Dou, Facile method to synthesize Na-enriched Na1+ x FeFe (CN) 6 frameworks as cathode with superior electrochemical performance for sodium-ion batteries, *Chemistry of Materials*, 2015, **27**, 1997-2003.
32 H. Zhang, J. Li, J. Liu, Y. Gao, Y. Fan, X. Liu, C. Guo, H. Liu, X. Chen and X. Wu, Understanding capacity fading from structural degradation in Prussian blue analogues for wide-temperature sodium-ion cylindrical battery, *Nature Communications*, 2025, **16**, 2520.
33 J. Pan, Y. Zhang, F. Sun, M. Osenberg, A. Hilger, I. Manke, R. Cao, S. X. Dou and H. J. Fan, *Angewandte Chemie International Edition*, 2023, **62**, e202219000.
34 L. Du, G. Xu, C. Sun, Y.-H. Zhang, H. Zhang, T. Dong, L. Huang, J. Ma, F. Sun and C. Li, *Nature Communications*, 2025, **16**, 2979.
35 X. Zhou, Y. Zhou, L. Yu, L. Qi, K.-S. Oh, P. Hu, S.-Y. Lee and C. Chen, Gel polymer electrolytes for rechargeable batteries toward wide-temperature applications, *Chemical Society Reviews*, 2024, **53**, 5291-5337.
36 W. Tang, R. Qi, J. Wu, Y. Zuo, Y. Shi, R. Liu, W. Yan and J. Zhang, Engineering, understanding, and optimizing electrolyte/anode interfaces for all-solid-state sodium batteries, *Electrochemical Energy Reviews*, 2024, **7**, 23.

View Article Online
DOI: 10.1039/D5SC08536E

The data that support the findings of this study are available from the author Fang Chen, chenfang01@zjenergy.com.cn, upon reasonable request.